Supplementary Information for:

Nanoscale-localized multiplexed biological activation of field effect transistors for biosensing applications

Alexander James Wright[1][†], Hashem Hassan Nasralla[1][†], Rahul Deshmukh[1], Moeid Jamalzadeh[2], Matthew Hannigan[3], Andrew Patera[4, 5], Yanxiao Li[1], Miguel Manzo-Perez[2], Nitika Parashar[1], Zhujun Huang[2], Thanuka Udumulla[5], Weiqiang Chen[6], Davide De Forni[7], Marcus Weck[3], Giuseppe Maria de Peppo[5], Davood Shahrjerdi[2*], Elisa Riedo1*

[1]Department of Chemical and Biomolecular Engineering, Tandon School of Engineering, New York University, Brooklyn, NY, 11201, USA

[2]Department of Electrical and Computer Engineering, Tandon School of Engineering, New York University, Brooklyn, NY, 11201, USA

[3]Department of Chemistry, New York University, New York, NY, 10003, USA

[4]Department of Cell Biology, SUNY Downstate Health Sciences University, Brooklyn, NY 11203, USA

[5]Mirimus, Inc, 760 Parkside Ave, Brooklyn, NY, 11226, USA

[6]Department of Biomedical Engineering, Tandon School of Engineering, New York University, Brooklyn, NY, 11201, USA

[7]ViroStatics S.r.l., Viale Umberto I, 46, 07100 Sassari, Italy

[†]These authors contributed equally to this work.

*Corresponding Authors: davood@nyu.edu, elisa.riedo@nyu.edu

List of Contents

Table S1: Comparison between different biofunctionalization methods for FET based biosensors.

Functionalization Method of FET	Spatially Selective Functionalization (YES/NO)	Spatial Resolution of Biofunctionalization	On-chip Multiplexing (Yes/No) Minimal Distance	Generalizability to Different Substrates?	Scalability of Multiplexing	CMOS Compatible	Reference
tSPL on Polymer	YES	15 nanometer	Yes, sub-micrometer	Yes	Yes	Yes	Our Work
Drop Casting	NO	N/A	Yes, few millimeters PDMS well	No (graphene only)	No	No	[1]
Drop Casting	NO	N/A	No	No (graphene only)	No	No	[2]
Drop Casting	NO	N/A	No	No (graphene only)	No	No	[3]
Drop Casting	NO	N/A	No	No (graphene only)	No	No	[4]
Drop Casting	NO	N/A	No	No	No	Yes	[5]
Drop Casting	NO	N/A	No	No	No	Yes	[6]
Drop Casting	NO	N/A	No	No (WSe$_2$ only)	No	Yes	[7]
Drop Casting	NO	N/A	Yes, few millimeters PDMS well	Yes (Silane Chemistry)	No	Yes	[8]
Drop Casting	NO	N/A	No	Yes (Silane Chemistry)	No	Yes	[9]
Drop Casting	NO	N/A	No	No	No	Yes	[10]
Drop Casting	NO	N/A	No	No	No	Yes	[11]
Drop Casting	NO	N/A	No	No (graphene only)	No	No	[12]
Drop Casting	NO	N/A	No	No (graphene only)	No	No	[13]
Drop Casting	NO	N/A	No	No (graphene only)	No	No	[14]
Electro-grafting	YES	50 micrometer	Yes, over one hundred micrometers	No (graphene only)	No	No	[15]
Photo-polymerization	YES	30 micrometer	100 micrometer	Yes	Yes	Yes	[16]

Table S2: Comparison between different biofunctionalization methods for non-FET based biosensors. [17-22]

Multiplexed Chemical Functionalization Method	Method of Detection	Size of Sensing Area	Number of Target Analytes	Reference
tSPL on Polymer	G-FET	20 x 40 μm	Scalable	Our Work
QD Microtiter Plates	QLISA/ELISA	6.35 mm well diameter	2-5	[17-19]
Injection-Molded Template	Plasmonic-based	300 x 300 μm	2-3	[20]
Non-contact Piezoelectric (Inkjet)	Photonic-based	50 x 50 μm	4	[21-22]

Supplementary Note 1: Reduction of non-specific binding using PPA

To reduce the non-specific binding outside of the patterned region, we cover the PMCC film with a PPA polymer film. We demonstrate this reduced non-specific binding by comparing the fluorescence data for the patterned PMCC film with and without PPA. Fig. S1 a and b below shows the fluorescence images for PMCC and PMCC/PPA stacks with 5μm squares patterned at intervals of 25°C. Both the samples are functionalized with NHS Biotin followed by Streptavidin tagged

with Dylight 633 dye. By observing the fluorescence intensity profiles along the dashed lines, we observe that the average floor of the intensity for the PMCC only sample is ~185 counts per sec, compared to 165 counts per sec for the PMCC/PPA stack, showing 11% reduction in fluorescence from non-specific binding.
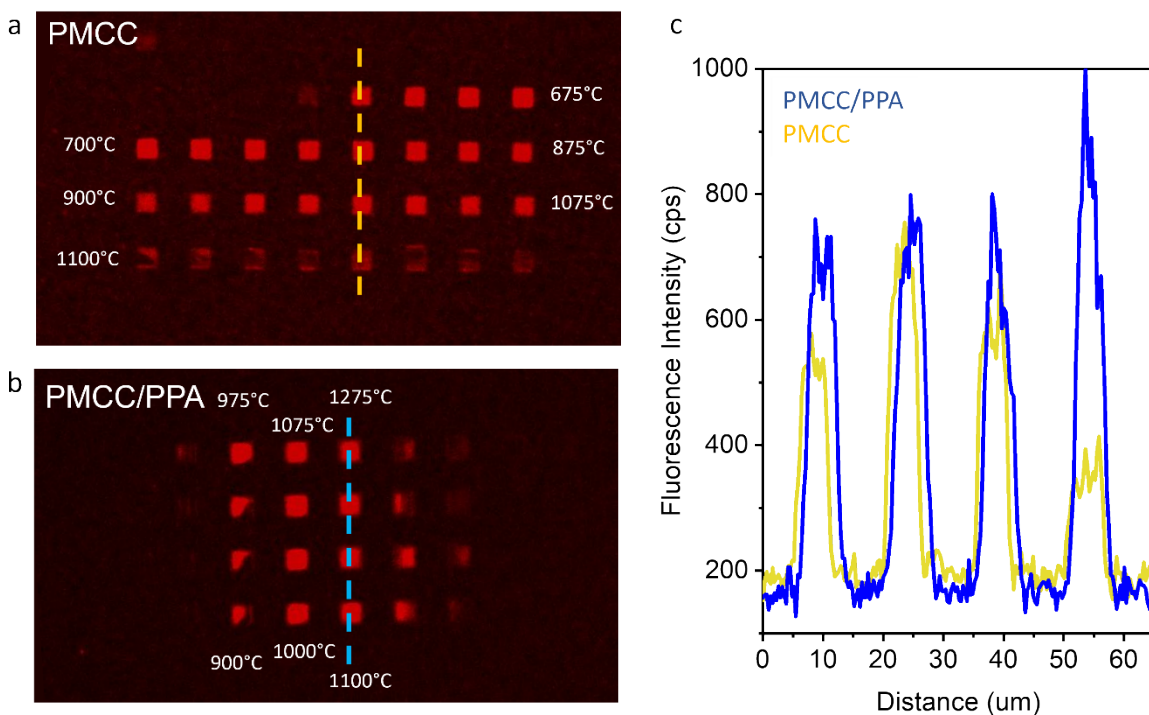

Fig. S1: Comparison of non-specific binding using fluorescence intensity analysis Comparison of samples with squares patterned at intervals of 25°C on a) PMCC and b) PMMC/PPA stack. c) shows the fluorescence intensity profiles along the dashed lines in panels a and b.

Supplementary Note 2: Electrical measurements of functionalized gFETs

gFET transient analyte buffers and injection procedure

As discussed in the main text, measurement buffers were chosen according to an appropriate Debye length for the specific measurement. Antibody experiments were performed in a 1 mM HEPES buffer containing 600 μM NaCl. Aptamer experiments were performed in 0.1x PBS buffer with 1 mM $MgCl_2$. Viral protein solutions were prepared in 1x PBS and diluted in the measurement buffer to the required concentration, resulting in a dilute but finite amount of PBS in the protein solutions. To account for this, and to mitigate spurious signals from small changes in buffer

salinity, protein solutions were diluted to maintain a constant PBS concentration, and an equal concentration was included in the measurement buffer.

gFET transient experiments commenced with an injection of 180 µL of the measurement buffer into the microfluidic chamber using a micropipette. Dilutions of the spike protein or viral samples were prepared in a matching buffer beforehand. The injections of viral suspensions were methodically administered, starting with 20 µL of the analyte to achieve the final virus concentration quoted in the main text.

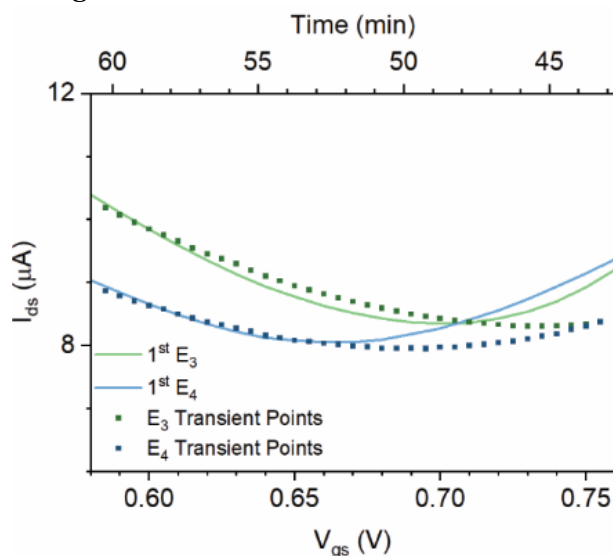*Stability Observations During Continuous Transient Measurements*

Fig. S2: Stability of gFET transfer characteristics. The steady-state drain current values from the transient $I_d(t)$ measurement shows the stability of the p-branch (left of minimum) and the distortion of the n-branch (right of minimum). The solid curves are obtained from I_{ds}-V_{gs} measurements, while the symbols represent the data from the transient measurement.

To study the stability of the gFETs, a gFET sample with no polymer coating was loaded into the microfluidic chamber with 0.01x PBS buffer. Two gFETs, E_3 and E_4, were measured. We conducted a transient measurement of I_{ds} and applied regular decremental changes to V_{gs}, recreating the shape of the characteristic transfer curve. Starting with an $V_g = 760$ mV, the system was allowed to stabilize (*i.e.*, the current reaches a constant minimum) and then the gate voltage was decremented in 50 mV steps every 30 seconds to 585 mV (sample rate 1 Hz). The I_{ds} values measured 15 seconds after change in V_{gs} were then graphed against the corresponding gate voltage

over the original characteristic curve, shown in Supplementary Fig. S2. The I_{ds} values obtained from the transient experiment overlap with the first characteristic curves of each electrode, as the surface discharged during the transient stabilization time. Notably, the p-branch of both characteristic curves match well with the data points, while we begin to see deviation on the n-branch beyond the charge neutrality points. As we are uncertain of the cause of this degradation, we use this as a rationale to conduct our electrical measurement experiments on the p-branch.

Estimated Limit of Detection

To estimate the limit of detection in our gFET devices, we perform analysis of the input-referred noise in the transient measurements. Supplementary Fig. S3a shows a ~5-minute interval of a transient measurement in which I_{ds} is stable, measured with the gFET of Fig. 3 of the main text,. We take the FFT to obtain the noise power spectrum shown in Supplementary Fig. S3b, revealing white noise to be the dominant source. Integrating over the band 0.01 Hz to 0.5 Hz gives an input-referred noise of 36 nA_{rms}, corresponding to a calibrated noise of 600 µV. Taking a signal-to-noise ratio of 3 as the lower limit for distinguishing a signal and using the calibration curve from Fig. 3e of the main text, we obtain a limit of detection of 1.9 aM.

Equivalently, for the gFET of Fig. 4 of the main text, we obtain an input-referred noise of 7.4 nA or 190 µV, from which we may estimate a limit of detection of 16 aM, although the scatter in the
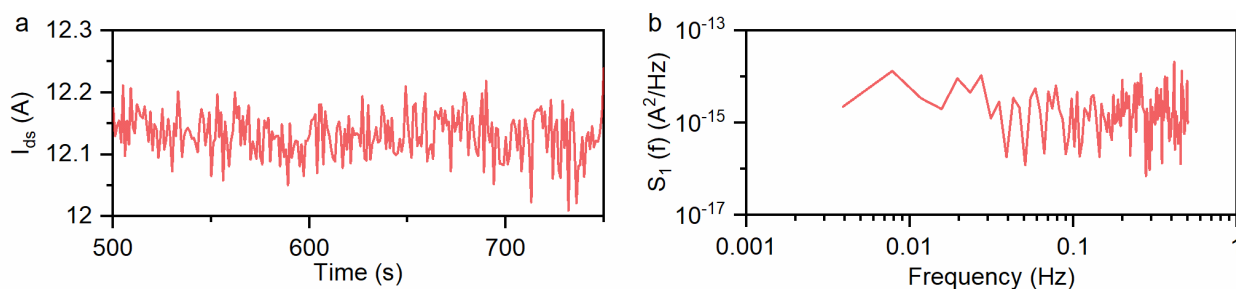
calibration plot gives less confidence in this value.

Fig. S3: Transient noise analysis. a Steady state transient measurement. **b** Noise power spectrum of (a) obtained by FFT.

Supplementary Note 3: Transfer and definition of graphene channels

Single layer graphene on copper foil from ACS Material is used for the graphene transfer. 2% PMMA in anisole is spin coated on a piece of the copper foil at 5000rpm for 60s, followed by soft-

bake on a hot-plate at 110°C for 2 mins. The copper is then etched in copper etchant (Sigma Aldrich) for 30 mins, leaving a graphene/PMMA stack, and washed 4 times by successive transfers to fresh DI Water baths using a glass microslide. This is followed by a final transfer onto the prepared substrate and dried for >12 hours. The PMMA layer is removed by UV exposure at 254 nm for 30 mins followed by chemical etching in acetone. The samples are dried using nitrogen and annealed in a tube furnace at 500°C (ramp rate ~5°C/min). in Ar/H_2 (100 scc/min flow rate) for 5 hours to remove PMMA residue.

To create the graphene channels, the graphene monolayers are spin-coated with 495 PMMA A11 (Kayaku), and islands regions are defined in the resist using electron beam lithography, developed in IPA:DI Water (3:1 ratio). 20nm gold is deposited in the patterned areas using electron beam evaporation to form a metal mask. The PMMA is removed in acetone and exposed graphene is removed by plasma cleaning in oxygen atmosphere for 10 mins. The samples are dipped in gold etchant for 10s to remove the gold masks, leaving the graphene islands. These islands are then inspected visually, and the best islands are used for fabricating the FETs in the second stage.

Supplementary Note 4: Nanoscale local biochemical functionalization

To ensure consistency in experimentation and avoid degradation of material, all functionalization solutions are prepared from stock vials the same day of the experiment. To avoid repetitive freeze-thaw cycles, stocks are aliquoted into smaller volumes before storage to maximize the lifespan of the materials. Eppendorf tubes used to prepare functionalization materials are vortexed to ensure proper dispersion throughout the volume, except for extremely low concentrations (< 1 nM); lower concentrations are mixed using pipettes and allowed to sit to disperse over time.

All solvents are acquired from Sigma-Aldritch, unless stated otherwise. The (+)-Biotin N-hydroxysuccinimide (NHS) ester, DyLight™-conjugated esters, streptavidin are acquired from ThermoFisher Scientific. Biotinylated Anti-SARS-CoV-2 Spike RBD Neutralizing Antibody (S1N-VM226), as well as SARS-CoV-2 spike proteins for detection are purchased from ACRO Biosystems. Aptamers are synthesized per order from Integrated DNA Technologies (IDT) using the following sequences from previous studies [23, 24]: Anti-SARS-CoV-2 Aptamer-6C3 5′-

CGCAGCAC CCAAGAAC AAGGACTG CTTAGGAT TGCGATAG GTTCGG-3′ (see Fig. S6) [23]. Anti-Hemagglutinin (HA) Aptamer-RHA-0006 (*Integrated DNA Technologies*, 5'-GGGTTTGG GTTGGGTT GGGTTTTT GGGTTTGG GTTGGGTT GGGAAAAA-3', see Fig. S7) [24]. Aptamers are modified with biotin on the 5' end and tagged with TYE™ 665 (Aptamer-6C3) or 6-Carboxyfluorescein (Aptamer-RHA-0006) fluorescent dye on the 3' end, formulated by Integrated DNA Technologies, Inc. [23, 25] and purified using high performance liquid chromatography (HPLC) [23].

In Fig. 2b, the study showcases the binding specificity of four different NHS-ester derivatives of DyLight Fluorophore to tSPL amine patterned shapes. These shapes are generated via tSPL on a PPA/PMCC coated Si/SiO2 chip. The process involves creating square, circle, star, and triangle patterns successively, each linked to a specific DyLight fluorophore by applying the respective DyLight NHS Ester in DMSO for 1 hour per pattern. The square patterns are formed initially using tSPL and then quenched with conjugated 100 nM DyLight™ 633 NHS Ester in DMSO (red fluorophore). Subsequently, each patterned shape undergoes a thorough wash in 1x PBS and DI-H_2O and drying with compressed N_2 gas to halt the amine-reaction. Utilizing *in-situ* tSPL imaging ensures precise and rapid patterning of designated geometries across multiple instances. This enables simultaneous imaging, facilitating the creation of aligned patterns with high-resolution registry (approximately 1 nm precision) after each functionalization step. Subsequent rounds involve the application of DyLight NHS Ester derivatives: 50 nM DyLight™ 550 for circles (orange-yellow fluorophore), 500 nM DyLight™ 405 for stars (blue fluorophore), and 200 nM DyLight™ 488 for triangles (green fluorophore). Each round follows the same process of tSPL patterning, functionalization, washing, and drying, resulting in distinct shapes corresponding to their designated fluorophores. Repeating rounds with alternative incubation produce patterns with different baits. Extended incubation time is used to ensure total coverage of the exposed amine sites to avoid "fluorescence bleeding" with subsequent ester additions.

Samples functionalized with aptamers (Fig. 1d, e, Fig. 2d-f, Fig. 4) or antibodies (Fig. 3, Fig. 5) follow the same functionalization procedure. After tSPL patterning, the sample is covered with 100 nM NHS-Biotin in DMSO and incubated, while covered, for 1 hour. The sample is then functionalized with 100 nM streptavidin in 1x PBS for 30 min. After another washing and drying step, the sample is functionalized with the desired biotinylated aptamers or antibody. Antibodies

are diluted to 100 nM in 1x PBS and incubated on the surface for 1 hour. Aptamers are prepared in nuclease-free distilled water to a dilution of 100 nM, heated at 95℃ for 5 min, and then allowed to cool to room temperature before application to ensure correct conformation. Aptamer-6C3 and Aptamer- RHA-0006 are incubated on the surface for 1 hour. After incubation of the bioreceptors, the sample is thoroughly washed in 1x PBS and DI water. In Fig. 2d-f this process is repeated twice for the two aptamers.

Supplementary Note 5: tSPL Parameters & Optimization

The NanoFrazor enables fully automated calibration routines and Python scripting, allowing for the rapid calibration of reading and writing parameters through the software. This includes the importing of various geometries, for layout writing, and patterning variables that control writing characteristics. The information provided will encompass several key parameters, but it is not exhaustive and may include additional relevant aspects; geometry import, pixel size, pixel time, heat pulse time, force pulse time, write force load, write temperature, depth feedback mode, forward height and height offset.

Geometry import and pixel size will determine the patterning shape and the dimensions of the target geometry. Pixel time, heat pulse time, and force pulse time while writing is the time interval between adjacent pixels, writer heating time for each pixel, and interval of force voltage applied between the cantilever and substrate for each pixel, respectively. The write temperature is the set temperature of the heater, not the temperature of the tip in contact with the polymer surface; this variable is translated to a voltage according to a measurement of the current-voltage (IV) characteristic for the cantilever during the calibration. The software uses an extrapolation of this measurement to adjust the applied voltage during patterning to maintain the desired set temperature. Depth feedback mode is used to optimize the writing force application during patterning according to different correlations. The forward height is the height of the tip from the surface when not writing; electrostatic forces are used to bring the tip in contact with the surface. The strength of the electrostatic forces and the tip contact temperature influence the depth of the patterning. Height offset compensates for the cantilever height during a reading scan.

The ability of the NanoFrazor to simultaneous read and write allows for the patterning of multiplexed samples (as shown in Fig. 1,2). In the case of Figure 2b, an entire image file is prepared in Illustrator, considering the desired pixel size, pattern sizes and pitch. Then, the said file will be exported to .bmp or .png files in grayscale four times; each time, the desired shape grayscale value will be set higher than the rest. The first image file is then imported into the software so that target geometry may be viewed. Setting the geometry to pattern as a 2D grayscale with an adequate threshold (50%) will remove all other shapes so that only one set of shapes would appear in the geometry field. The finalized field is imported into a new layout for later patterning. Following this, each of the other image files are imported the same way, presenting each of the different shape grids in the geometry field. Importing each of these fields in the same layout as the first will create sub-fields that are actively selected or deselected when patterning.

The patterning of Figure 2b began with the square grid in a desired area by selecting only the first sub-field in the new layout. Post functionalization, the same area was found optically before the piezo approach and cantilever configuration. The area is then scanned with a large read field so that the previously patterned squares appear in the world map (a tool that overlays the optical camera with existing scanned topography for reference). Switching to writing, the shapes are maneuvered by manipulating both the layout position and angle as to perfectly overlay the previously patterned squares, as per the scanned topography) with the total layout. As each sub-field is independent from one another, the undesired fields (i.e. the squares) are then deselected so that only the next shape (i.e. the circles) will be patterned. This same process is repeated post each functionalization step until the figure is complete. The same principles are applied to create Fig 2d-f.
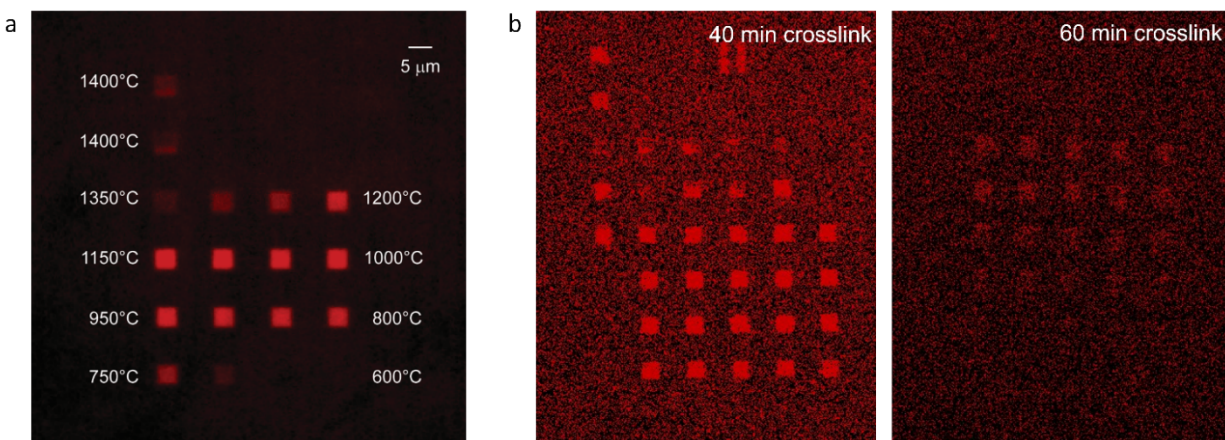
Fig. S4: Optimization of amine exposure through fluorescence imaging. (a) Temperature optimization: The fluorescence image of patterned 5 μm squares in a grid with write temperatures ranging from 600°C to 1400°C (in steps of Δ50°C), a dwell time of 120 μs, and a load of 6.5 V. (b) UV crosslink time optimization: Fluorescence images of patterned 5 μm squares in PMCC samples crosslinked for 40 mins and 60 mins.

Supplementary Note 6: Calibration of sensor response

The transient measurements in the main manuscript are performed by measuring I_{ds} at fixed V_{gs}. Capture of an analyte changes the charge at the sensor surface, producing a shift in the $I_{ds}(V_{gs})$ characteristics, that is detected as a change in the measured I_{ds}. To demonstrate this, we show an exaggerated example in Fig. S5 in which the initial $I_{ds}(V_{gs})$ characteristics are plotted. After analyte capture, the transfer characteristics are shifted by ΔV_{CNP} and the drop in I_{ds} can be seen, indicated by ΔI_{ds}. The magnitude of ΔI_{ds} depends on the transconductance of the sensor, $g_m = dI_{ds}/dV_{gs}$, plotted in the bottom panel of Fig. S5. Clearly, g_m varies strongly depending on the change in V_{CNP}, and will vary between devices; measured ΔI_{ds} values will also vary. To account for this, we perform a phenomenological fit to the g_m data as a function of I_{ds}, and obtain a calibrated sensor signal $\Delta I_{ds}/g_m(I_{ds})$. In this way, the reported sensor signal is independent of the device characteristics.
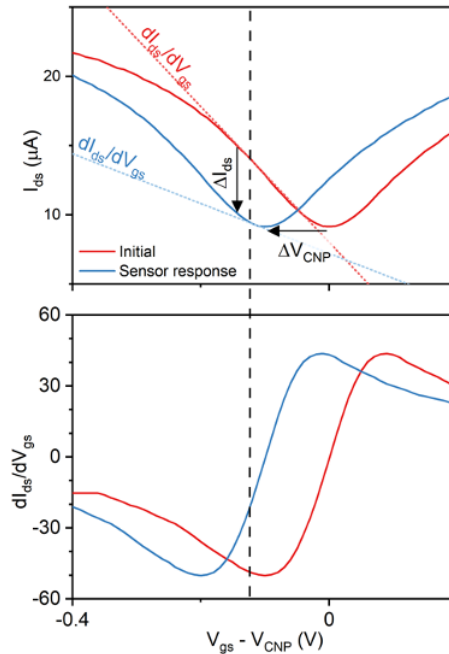
Fig. S5: Calibration of sensor response (Top panel) Initial $I_{ds}(V_{gs})$ characteristics of a sensor centered at V_{CNP} shown in red. After a response of the sensor to an analyte, the characteristics are shifted by ΔV_{CNP} shown in blue. At fixed V_{gs} (vertical dashed line), there is a corresponding change in I_{ds} indicated by ΔI_{ds}. (Bottom panel) Transconductance of the sensor corresponding to the lines in the top panel.

Output of sir_graph (©)
mfold_util 4.7

dG = -4.70 Aptamer-6C3

Fig. S6: Modeled structure of SARS-CoV-2 Aptamer. Secondary structure modeled two-hairpin prediction for the SARS-CoV-2 Aptamer-6C3 using the mfold software [25]. The aptamer is modified with biotin on the 5' end and tagged with TYE™ 665 fluorescent dye on the 3' end.
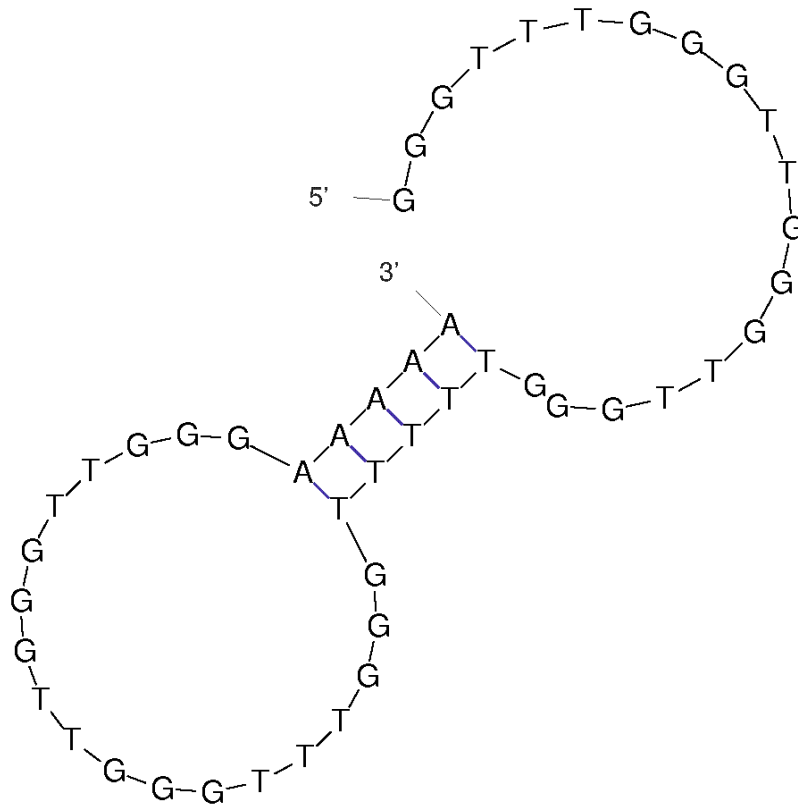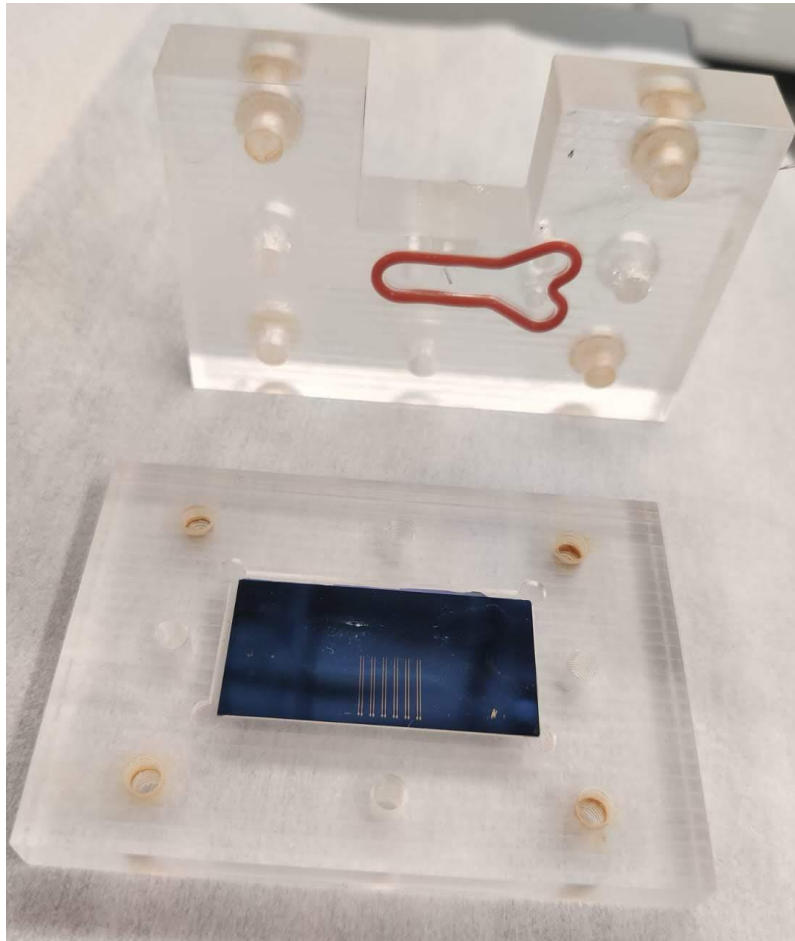
dG = 0.65 Aptamer-RHA0006

Fig. S7: Modeled structure of HA Aptamer. Secondary structure modeled two-hairpin prediction for the Hemagglutinin Aptamer-RHA0006 using the mfold software [25]. The aptamer is modified with biotin on the 5' end and tagged with 6-Carboxyfluorescein fluorescent dye on the 3' end.
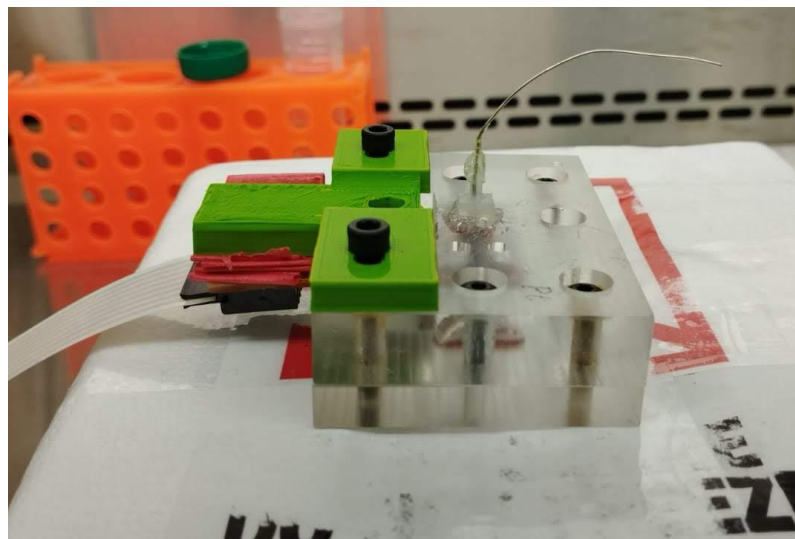
Fig. S8: Microfluidic chamber: (top) The two halves before closing for experiments and (bottom) during electrical measurements.
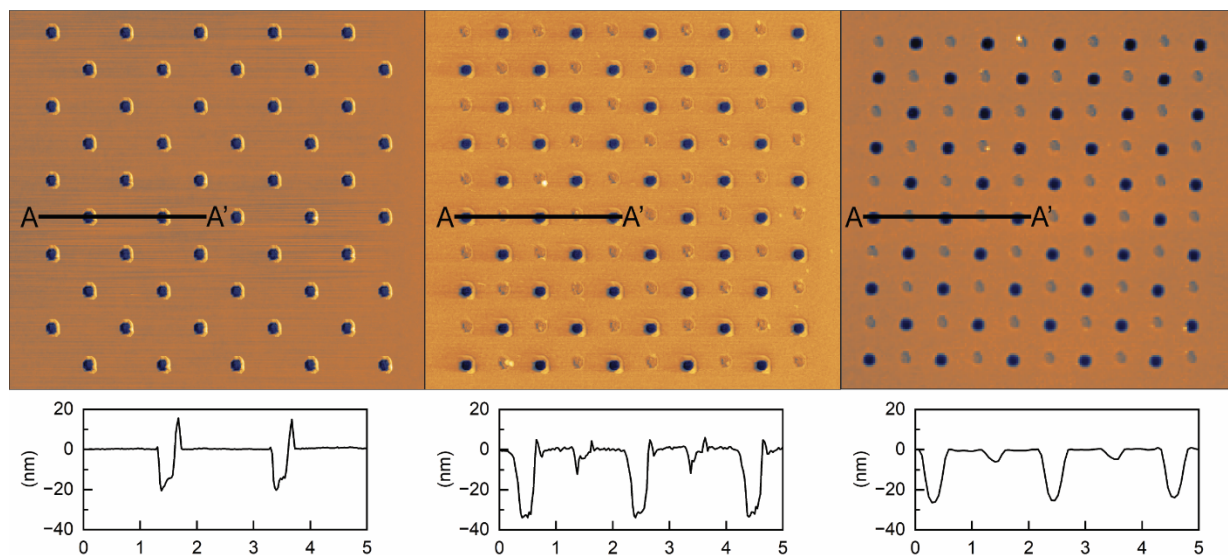
Fig. S9: **Topographical data at different stages of functionalization.** From left to right: first, *in-situ* tSPL topographical image of a matrix of 250 nm circles produced after a first round of tSPL on a PPA/PMCC/SiO$_2$/Si chip; second, *in-situ* tSPL topographical image of the same area after conjugation of the surface with bioreceptor 1 (CoV-2 aptamer) using biotin/streptavidin as cross linker and after a second round of tSPL to pattern a second matrix of 250 nm circles (deeper circles); third, *ex-situ* AFM topographical image of the same area after conjugation of bioreceptor 2 (HA aptamer) using biotin/streptavidin as cross linker. The respective cross section images show the registry and robustness of multiplexed patterning and the change in depth of the patterns after functionalization due to the filling of each pattern with the NHS-biotin/streptavidin/aptamer molecules (approximately 10 -15 nm).
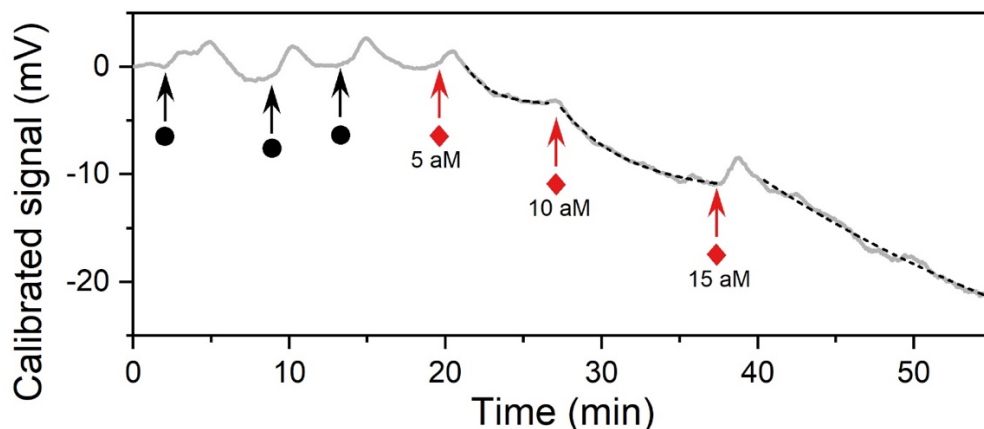
Fig. S10: **Additional transient response of antibody-modified gFET.** Spike protein injections for an antibody-modified gFET device. We initially perform repeated injections of the buffer solution (black circles) and monitor the gFET's response. The purpose of these injections is to record possible artifacts which might contribute to a false sensor response. Although each injection of the buffer solution generates a small detectable response, they are consistent among the three injections and, more critically, do not cause a permanent shift in the signal baseline. These observations give confidence that the artifacts of the injection process are negligible and temporary, and thus do not contribute to the steady-state sensor response due to the antibody-spike protein interactions. We then perform injections of spike protein (red diamonds) at increasing concentrations, indicated in the figure, which produce a strong decrease in the signal baseline. The first two spike protein responses are included in the sensitivity plot in Figure 3e of the main manuscript. The third injection does not saturate within the measurement, and is therefore not included.
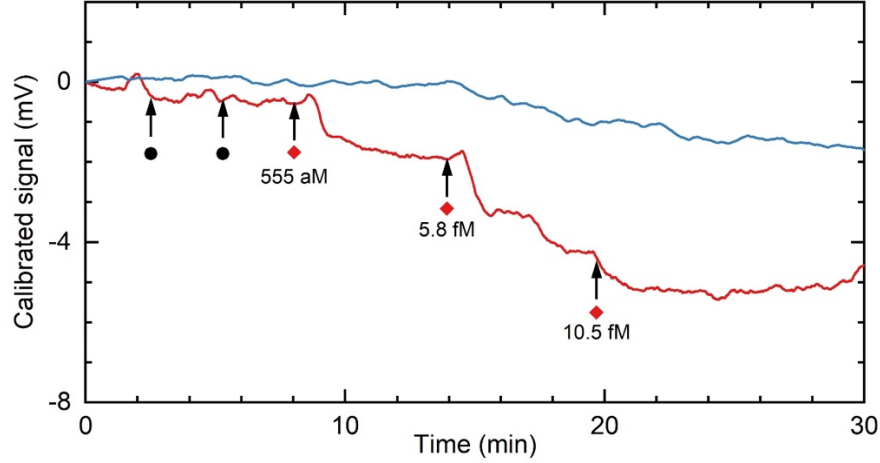
Fig. S11: **Additional transient response of aptamer-modified gFET.** Spike protein injections for an aptamer-modified gFET device. Buffer injections (black circles) produce negligible response. Spike protein injections (red diamonds) produce a drop in the sensor current. Signal responses are included in the sensitivity plot in Figure 4e of the main text.
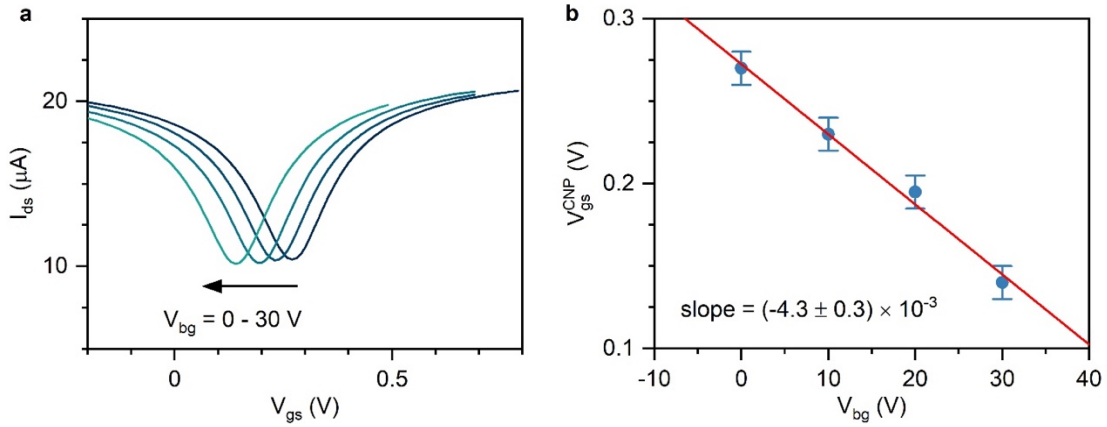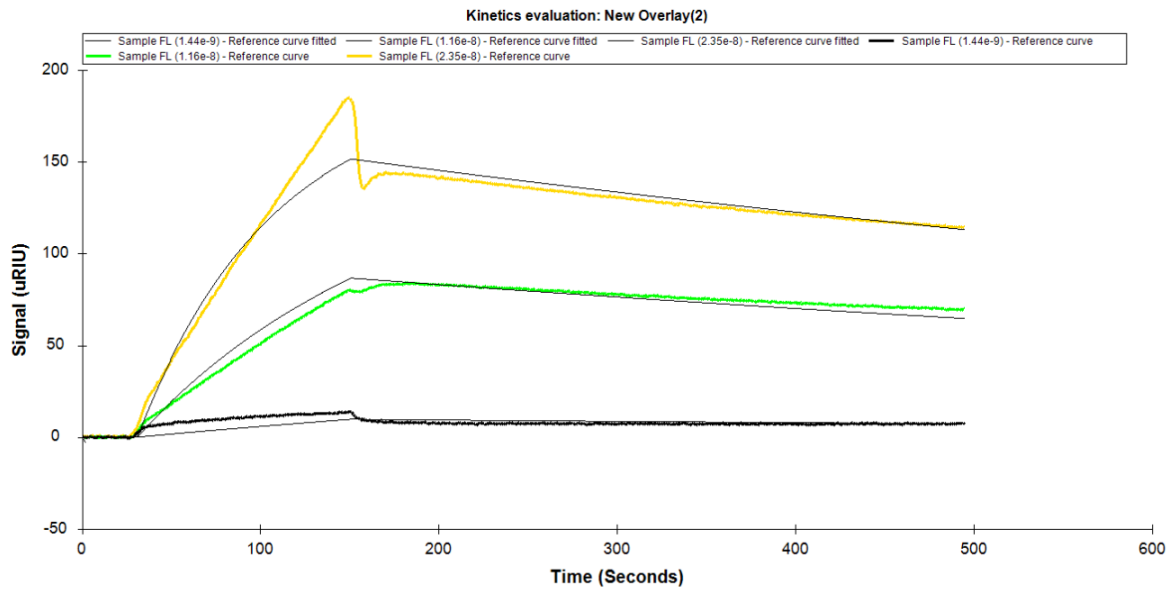

Fig. S12: PMCC Polymer capacitance in hydrate state. a) The solution-gated transfer characteristics of a PMCC-coated gFET device in a buffer solution at different back-gate voltages V_{bg}. In these experiments, I_{ds} was measured by sweeping the top gate bias (V_{gs}) at different V_{bg} steps. b) Charge neutrality points (V_{gs}^{CNP}) from panel (a) as a function of V_{bg}. The slope of the linear fit to the data provides the ratio of the back-gate to top-gate capacitances $\Delta V_{g,ionic}^{CNP}/\Delta V_{bg} \approx C_{bg}/C_{tg}$ [26]. For 285 nm thick SiO_2, C_{bg} = 11 nF/cm^2, hence we find C_{tg} = 2.6 μF/cm^2. Such a large capacitance is consistent with an increase in the relative permittivity of the polymer due to hydration, which has been shown to occur in other polymer films [27]. A more detailed investigation into the electrical characteristics of this polymer will be the subject of later work.

Fig. S13: **Kinetic analysis of the SPR data.** The SPR data obtained for interactions of spike protein with (top) aptamer and (bottom) antibody at 1 mM HEPES buffer solution. While the data validate the affinity, the artifacts due to low ionic concentrations impede the reliable analysis of kinetics of affinities.

References

1. Kumar, N., et al., *Graphene Field Effect Biosensor for Concurrent and Specific Detection of SARS-CoV-2 and Influenza.* ACS nano, 2023. **17**(18): p. 18629-18640.
2. Fenoy, G.E., et al., *The effect of amino–phosphate interactions on the biosensing performance of enzymatic graphene field-effect transistors.* Analytical Chemistry, 2022. **94**(40): p. 13820-13828.
3. Piccinini, E., et al., *Biofunctionalization of Graphene-Based FET Sensors through Heterobifunctional Nanoscaffolds: Technology Validation toward Rapid COVID-19 Diagnostics and Monitoring.* Advanced Materials Interfaces, 2022. **9**(15): p. 2102526.
4. Seo, G., et al., *Rapid detection of COVID-19 causative virus (SARS-CoV-2) in human nasopharyngeal swab specimens using field-effect transistor-based biosensor.* ACS nano, 2020. **14**(4): p. 5135-5142.
5. Ping, J.L., et al., *Scalable Production of High-Sensitivity, Label-Free DNA Biosensors Based on Back-Gated Graphene Field Effect Transistors.* Acs Nano, 2016. **10**(9): p. 8700-8704.
6. Xu, L., et al., *On-chip integrated graphene aptasensor with portable readout for fast and label-free COVID-19 detection in virus transport medium.* Sens Diagn, 2022. **1**(4): p. 719-730.
7. Fathi-Hafshejani, P., et al., *Two-dimensional-material-based field-effect transistor biosensor for detecting COVID-19 virus (SARS-CoV-2).* ACS nano, 2021. **15**(7): p. 11461-11469.
8. Nakatsuka, N., et al., *Aptamer–field-effect transistors overcome Debye length limitations for small-molecule sensing.* Science, 2018. **362**(6412): p. 319-324.
9. Duan, X., et al., *Quantification of the affinities and kinetics of protein interactions using silicon nanowire biosensors.* Nature nanotechnology, 2012. **7**(6): p. 401-407.
10. Capua, L., et al., *Label-Free C-Reactive Protein Si Nanowire FET Sensor Arrays With Super-Nernstian Back-Gate Operation.* Ieee Transactions on Electron Devices, 2022. **69**(4): p. 2159-2165.
11. Dai, C., et al., *Ultraprecise antigen 10-in-1 pool testing by multiantibodies transistor assay.* Journal of the American Chemical Society, 2021. **143**(47): p. 19794-19801.
12. Piecinini, E., et al., *Enzyme-polyelectrolyte multilayer assemblies on reduced graphene oxide field-effect transistors for biosensing applications.* Biosensors & Bioelectronics, 2017. **92**: p. 661-667.
13. Silvestri, A., et al., *Ultrasensitive detection of SARS-CoV-2 spike protein by graphene field-effect transistors.* Nanoscale, 2023. **15**(3): p. 1076-1085.
14. Rodrigues, T., et al., *Highly performing graphene-based field effect transistor for the differentiation between mild-moderate-severe myocardial injury.* Nano Today, 2022. **43**.
15. Gao, Z., et al., *Multiplexed Monitoring of Neurochemicals via Electrografting-Enabled Site-Selective Functionalization of Aptamers on Field-Effect Transistors.* Analytical Chemistry, 2022. **94**(24): p. 8605-8617.
16. Bay, H.H., et al., *Hydrogel Gate Graphene Field-Effect Transistors as Multiplexed Biosensors.* Nano Letters, 2019. **19**(4): p. 2620-2626.
17. Xu, L., et al., *Development of quantum dot-linked immunosorbent assay (QLISA) and ELISA for the detection of sunset yellow in foods and beverages.* Food Chemistry, 2022. **385**: p. 132648.
18. Song, E., et al., *Multi-color quantum dot-based fluorescence immunoassay array for simultaneous visual detection of multiple antibiotic residues in milk.* Biosensors and Bioelectronics, 2015. **72**: p. 320-325.
19. Jarockyte, G., et al., *Multiplexed Nanobiosensors: Current Trends in Early Diagnostics.* Sensors, 2020. **20**(23): p. 6890.
20. Wallace, S., et al., *Multiplexed Biosensing of Proteins and Virions with Disposable Plasmonic Assays.* ACS Sensors, 2023. **8**(9): p. 3338-3348.
21. Kirk, J.T., et al., *Multiplexed inkjet functionalization of silicon photonic biosensors.* Lab on a Chip, 2011. **11**(7): p. 1372-1377.
22. Puumala, L.S., et al., *Biofunctionalization of Multiplexed Silicon Photonic Biosensors.* Biosensors, 2023. **13**(1): p. 53.

23. Sun, M., et al., *Aptamer Blocking Strategy Inhibits SARS-CoV-2 Virus Infection.* Angewandte Chemie-International Edition, 2021. **60**(18): p. 10266-10272.

24. Shiratori, I., et al., *Selection of DNA aptamers that bind to influenza A viruses with high affinity and broad subtype specificity.* Biochemical and Biophysical Research Communications, 2014. **443**(1): p. 37-41.

25. Zuker, M., *Mfold web server for nucleic acid folding and hybridization prediction.* Nucleic Acids Research, 2003. **31**(13): p. 3406-3415.

26. Kim, S., et al., *Realization of a high mobility dual-gated graphene field-effect transistor with Al2O3 dielectric.* Applied Physics Letters, 2009. **94**(6).

27. Joh, D.Y., et al., *Poly(oligo(ethylene glycol) methyl ether methacrylate) Brushes on High-κ Metal Oxide Dielectric Surfaces for Bioelectrical Environments.* ACS Applied Materials & Interfaces, 2017. **9**(6): p. 5522-5529.